CIRP Journal of Manufacturing Science and Technology 55 (2024) 42–53

Contents lists available at ScienceDirect

CIRP Journal of Manufacturing Science and Technology

journal homepage: www.elsevier.com/locate/cirpj

# Influence of the process parameters on the microstructure and the machinability of additively manufactured Ti-5553 titanium alloy

Berend Denkena [a], Julia K. Hufenbach [b,c], Benjamin Bergmann [a], Uta Kühn [b], Arnd Heckemeyer [a], Sebastian Worpenberg [a,1], Clemens Kunz [b,1,*]

[a] Institute of Production Engineering and Machine Tools (IFW), Leibniz Universität Hannover, An der Universität 2, 30823 Garbsen, Germany
[b] Leibniz Institute for Solid State and Materials Research Dresden, Helmholtzstraße 20, D-01069 Dresden, Germany
[c] Institute of Materials Science, TU Bergakademie Freiberg, Gustav-Zeuner-Str. 5, D-09599 Freiberg, Germany

ARTICLE INFO

*Keywords:*
Additive manufacturing
Ti-5553
Microstructure
Material properties
Milling
Tool wear

ABSTRACT

Additive Manufacturing (AM) technologies, particularly laser powder bed fusion (LPBF), are revolutionising the production of complex geometries and lightweight structures. Furthermore, LPBF allows to tailor the microstructure and resulting properties of metallic materials. This study focuses on titanium alloys, crucial for high-performance applications like aircraft components and medical implants. Although AM enables near-net-shape fabrication, many titanium parts still require machining to meet surface and dimensional standards. Titanium's challenging machinability is well-documented for cast and wrought alloys, but only less is known about additively manufactured variants. In this work, the machinability of an additively manufactured Ti-5Al-5V-5Mo-3Cr alloy (Ti-5553) is investigated, focusing on chip formation, cutting forces, and tool wear across different LPBF process parameters. Four LPBF parameter sets were validated, and results were compared to conventional wrought sample. The findings reveal significant variations in machinability linked to LPBF parameters. Specifically, the highest tool loads and wear were observed for samples produced with the highest energy density of $E_V$ = 37.0 J/mm$^3$, likely due to α-phase precipitation. In contrast, samples with lower energy densities (<29.1 J/mm$^3$) exhibited up to 100% longer tool life. Concluding, this study highlights how the machinability of Ti-based components can be significantly influenced by the LPBF processing parameters.

## 1. Introduction

Additive manufacturing (AM) has emerged as a revolutionary technique in the fabrication of components across various industries. The layer-by-layer buildup process based on a digital model allows the production of near-net-shaped parts with complex geometries [1–5]. Currently, the most dominant metal AM technology is laser powder bed fusion (LPBF). In this process, the respective metal powder is melted using high-energy laser radiation. By selecting suitable process parameters, dense, crack-free, low-distortion, cost-efficient, and complex components can be manufactured [1,6–9]. There are a variety of variables for the process that impact the resulting microstructure and, consequently, the subsequent material properties. In addition to factors dependent on powder properties and machine types, the chosen laser parameters exert the greatest influence. These are combined in the literature [5,10] into a so-called energy density ($E_V$, unit J/mm$^3$), which is calculated using the following Equation:

$$E_V = \frac{P_L}{h_S \bullet l_Z \bullet v_S} \quad (1)$$

Here, $P_L$ represents the average laser power, $h_s$ denotes the hatch distance, $l_z$ signifies the applied powder layer thickness, and $v_s$ represents the scanning speed og the laser beam. The volumetric energy density plays a significant role in shaping density, surface topography, and microstructure [11–13]. Additional influences may arise from the chosen laser wavelength, operating mode (pulsed or continuous), the incident beam profile of the laser, and the focal spot diameter of the laser beam on the AM process [10,12,14–19]. Manufacturing via laser radiation results in extremely high heating and cooling rates ($10^3$ - $10^8$ K/s [20]). It can be assumed that the samples are produced in a non-thermodynamically stable equilibrium, thus allowing the formation of unstable material phases. Apart from the formation of various phases,

* Corresponding author.
*E-mail address:* c.kunz@ifw-dresden.de (C. Kunz).
[1] Contributed equally

https://doi.org/10.1016/j.cirpj.2024.09.002
Received 30 April 2024; Received in revised form 30 July 2024; Accepted 1 September 2024
Available online 11 September 2024

other factors also exert influence on material properties. These factors encompass the structure, density, residual stresses, and surface topography [21–23].

In principle, with the help of LPBF and the appropriate selection of parameters, a broad range of metallic materials can be processed. In the literature, materials ranging from iron-based, nickel-based, aluminum-based, titanium alloys, and many more can be found [24]. Titanium alloys are prized for their exceptional strength-to-weight ratio, corrosion resistance, and biocompatibility, making them indispensable in critical sectors such as aerospace, medical, and automotive industries [25–29]. The versatility and precision offered by AM technology have opened new avenues for the production of complex geometries and customized parts with enhanced performance characteristics. For example, Pilz *et al.* [19] demonstrated that by deliberately altering process parameters, various microstructural modifications could be achieved. The components thus manufactured exhibited optimized mechanical properties suitable for subsequent medical applications.

Despite the potential for near-net-shape production offered by the LPBF process, surface finishing of components is often necessary. Typically, semi-finished products exhibit uneven surfaces with high levels of roughness. To meet dimensional accuracy requirements, especially for functional surfaces, milling or turning operations are employed. Titanium, renowned for its exceptional mechanical properties and low density, also has low thermal conductivity. Consequently, during machining, a considerable amount of heat generated is dissipated through the cutting edge, leading to significant wear and reduced tool lifespan [30].

Due to the wide range of material properties and AM processes, a large number of publications on the machinability of additively manufactured materials can be found in the literature [31–35]. Studies on titanium mostly focus on the popular (α + β)-alloy Ti-6Al-4V [36]. Additively manufactured titanium alloys are usually found to have a higher hardness and tensile strength than conventionally manufactured alloys, which reduces the machinability. This is indicated by higher cutting forces and higher process temperatures, which leads to increased tool wear. Furthermore, the analysis of AM titanium chips shows a pronounced shear chip formation due to adiabatic shearing [30,37]. However, at low cutting speeds, the machinability of wrought titanium alloys is comparable to that of AM titanium. Uçak *et al.* [38] also point out that a specific process design must be carried out for machining AM titanium and that the transferability of milling processes for wrought alloys to AM titanium is only possible with considerable restrictions.

The material investigated in our study is a near-β titanium alloy with the composition Ti-5Al-5V-5Mo-3Cr (Ti-5553). These alloys consist mainly of the β-phase, which is characterized by a cubic crystal system and has a good deformability. Through heat treatment above the β-transus temperature, α-phases can form in various morphologies (globular, plate-like) [39]. The α-phase has a hexagonal crystal system and acts as a strengthening phase. By deliberately adjusting the α-content in the β-matrix, excellent mechanical properties can be achieved [40–42]. Compared to the commonly used titanium alloy Ti-6Al-4V, machining Ti-5553 is expected to be more challenging. Grove *et al.* [43] previously explored the effects of various microstructure modifications resulting from different AM process parameters on chip formation, process forces, and tool wear. A comparison between conventionally manufactured material and additively manufactured samples, with and without in-process heat treatment, revealed notable differences. Machining the additively manufactured sample with in-process heat treatment resulted in significantly higher tool wear and process forces compared to both the reference material and the additively manufactured sample in its original as-built condition. For β-near alloys like Ti-5553, it has been observed that the formation of the α-phase can be inhibited due to the elevated cooling rates during LPBF, thereby stabilizing a pure β-phase composition even at room temperature [16,44].

In this study, we aim to explore the influence of laser parameters during the LPBF process on tool wear during subsequent milling operations. Our goal is to enhance the understanding of the machinability of this alloy in relation to the LPBF process parameters. To achieve this, Ti-5553 samples are produced using various LPBF process parameters, resulting in different microstructures without additional heat treatment. Subsequently, wear tests are conducted during the milling of these materials and compared with wear test results on wrought Ti-5553 material.

## 2. Experimental setup

### 2.1. Material processing and analysing

The scope of the analyses is based on additively manufactured Ti-5553, which was produced with different sets of parameters. To compare the material properties and machinability with conventional Ti-5553, all analyses were also carried out on a wrought alloy, which is labelled below as a reference. The Ti-5553 samples produced via additive manufacturing were fabricated using an SLM-280 2.0 dual system from SLM-Solutions at the Leibniz Institute for Solid State and Materials Research Dresden. The utilized powder is characterized by a particle size distribution ranging from 25 µm to 55 µm (spherical shape, $d_{50}$ = 41.9 µm, CamSizer X2, Retsch Technologies), manufactured via the Electrode Induction Melting Inert Gas Atomization (EIGA) process at ECKART TLS.

The chemical compositions of the reference material (wrought and heat treated, Otto Fuchs), additively manufactured Ti-5553 with the highest energy input, and the Ti-5553 powder are provided in Table 1. The chemical analysis was conducted using inductively coupled plasma optical emission spectroscopy (ICP-OES, IRIS Intrepid II XUV, ThermoFisher Scientific) for metallic elements and carrier gas hot extraction (EMIA 820 V, Horiba) for non-metallic elements.

In this study, four different parameter sets for the LPBF process were utilized, summarized in Table 2, encompassing laser process parameters, resulting energy density, and volume rate of the manufacturing process. The layer thickness ($l_Z$) for all processes is 90 µm, with a gaussian laser beam profile approximately 80 µm in diameter. Before finalizing the parameters for this study, preliminary parameter optimizations were conducted. The goal was to produce samples that were as crack-free, distortion-free, and dense as possible, while achieving high build rates. This approach ensured a sufficient number and size of samples for later analyses. The final surface qualities, such as roughness, were considered of secondary importance since they were removed before the actual machining tests.

For each set of process parameters in the LPBF process, samples were fabricated for milling tests and for assessing mechanical properties and microstructure. The manufactured blocks for all tests were sized $(20 \times 30 \times 50)\ mm^3$, with the largest dimension oriented in the build-up direction. To ensure the reproducibility of the additive samples, the respective parameters were always applied in a common build job after finalizing the parameters. The components were always manufactured under the same conditions, such as an oxygen content below 0.05% and a build plate temperature of 80 °C, etc. Additionally, various random samples (not shown here) were taken during the experiments to verify the resulting microstructures and properties. Furthermore, the same rectangular shape used in machining $(20 \times 30 \times 50)\ mm^3$ was employed for subsequent analyses, and the required sample shapes were obtained via wire electrical discharge machining. This maintained consistent temperature conditions during building through constant vector length during exposure to the laser beam. Extensive characterization of the samples was conducted, including compression and tensile tests, microhardness measurements, microstructure analysis via electron backscatter diffraction (EBSD), and qualitative phase analysis using X-ray diffraction (XRD).

Tensile tests were conducted with four tensile samples per AM parameter set on an Instron 8502 servo-hydraulic testing machine at a

**Table 1**
Nominal composition (datasheet from reference supplier Otto Fuchs) and chemical analysis of Ti-5553-powder, conventionally and additively manufactured Ti-5553.

| Element content [wt%] | Ti | Al | Mo | V | Cr | Fe | Cu | O | C | N |
|---|---|---|---|---|---|---|---|---|---|---|
| Nominal composition | bal. | 4.4 - 5.7 | 4.0 - 5.5 | 4.0 - 5.5 | 2.5 - 3.5 | 0.3 - 0.5 | - | ≤ 0.18 | ≤ 0.1 | ≤ 0.05 |
| Reference Ti−5553 | bal. | 5.57 ± 0.05 | 4.81 ± 0.07 | 4.96 ± 0.03 | 2.95 ± 0.04 | 0.40 | (0.35) | 0.132 | 0.0041 | 0.0037 |
| Ti−5553 powder | bal. | 4.90 ± 0.05 | 4.82 ± 0.02 | 4.68 ± 0.02 | 2.88 ± 0.02 | 0.36 | - | 0.130 | 0.0102 | 0.0144 |
| Additively manufactured Ti−5553 (37.0 J/mm$^3$) | bal. | 4.82 ± 0.05 | 4.84 ± 0.06 | 4.70 ± 0.03 | 2.82 ± 0.03 | 0.40 | (0.20) | 0.146 | 0.0085 | 0.0229 |

**Table 2**
Process parameters of the LPBF process and resulting energy density and volume rate.

| Sample name | Average laser power $P_L$ [W] | Hatch distance $h_s$ [mm] | Scanning speed $v_s$ [mm/s] | Energy density $E_V$ [J/mm$^3$ ] | Volume rate $V$ [mm$^3$ /s] |
|---|---|---|---|---|---|
| 20.8 J/mm$^3$ | 550 | 0.21 | 1400 | 20.8 | 26.5 |
| 29.2 J/mm$^3$ | 600 | 0.19 | 1200 | 29.2 | 20.5 |
| 32.7 J/mm$^3$ | 550 | 0.17 | 1100 | 32.7 | 16.8 |
| 37.0 J/mm$^3$ | 550 | 0.15 | 1100 | 37.0 | 14.9 |

strain rate of $0.5 \cdot 10^{-4} \cdot 1/s$, following the specimen geometry type B of DIN 50125:2016. Compression tests were performed on cylindrical specimens with dimensions of 3 mm in diameter and 6 mm in height, according to DIN 50106, using an Instron 5869 at a constant strain rate of $10^{-3} \cdot 1/s$ (six samples per parameter set). Microhardness measurements were carried out according to Vickers (DIN EN ISO 6507) with 30 hardness impressions on a Shimadzu HMV-2 micro hardness tester, using a measuring force of 1.961 N (HV 0.2). Density measurements during parameter optimization were conducted on $(10 \times 10 \times 10)$ mm$^3$ cubes using a density balance (MSA225S, Sartorius) with distilled water based on the Archimedes principle. The measurements were repeated three times on different days to ensure the samples were dried properly.

EBSD analysis was conducted using a Zeiss Leo 1530 Gemini microscope with a Bruker eFlash detector, in conjunction with Esprit 2.5 Software. Samples for EBSD analysis were prepared by grinding and polishing with colloidal silicon dioxide EPOSIL M11 (QATM). During the analysis, an acceleration voltage of 20 kV was used, with an EBSP resolution of $120 \times 120$ and exposure times between 10–15 ms. The magnification was set in all analyses to 80x with a pixel-size of 1 µm. XRD measurements were performed using an X-ray diffractometer Stadi P from STOE in transmission mode with Mo-Kα radiation and a Mythen 1 K detector. For XRD analysis in transmission mode, samples were ground to 40 to 60 µm thick discs using P4000 grit.

### 2.2. Milling tests

The mechanical tool load was investigated by milling tests on the Ti-5553 samples. The experimental investigations were carried out on a Heller H5000 4-axis machine tool using a Seco R217.69–1010.0-06–2AD milling cutter with solid carbide indexable inserts Seco XOMX060208R-M05 F40M (Fig. 1). The tool has two teeth and a diameter of 10 mm. The used carbide grade F40M has a (Ti,Al)N-TiN PVD-coating and is used for fine to medium rough milling and with small feeds and low cutting speeds. It is recommended for milling superalloys. To minimize vibrations during milling, a short hydraulic expansion toolholder of type Schunk Tendo E compact was used. The process forces were measured

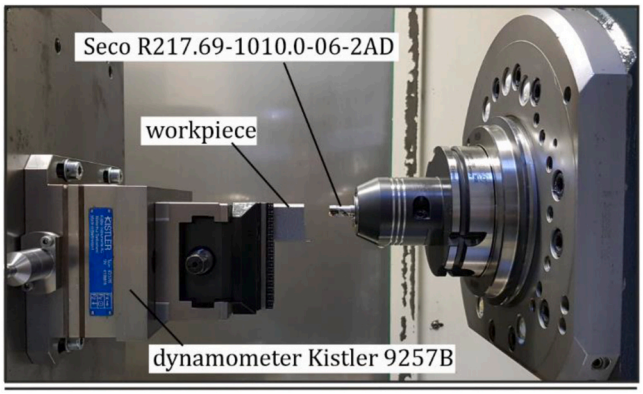


**Fig. 1.** Experimental setup and summary of the process parameters used for milling tests.

on a Kistler 3-component dynamometer of the type 9257B.

The milling tests were carried out with a cutting speed $v_c$ of 80 m/min and a feed per tooth $f_z$ of 0.06 mm. These values are based on recommendations from Seco Tools for milling titanium alloys with the specific tool. All tests were performed with a depth of cut of $a_p = 1$ mm and a width of cut $a_e = 1.5$ mm in side milling and down milling. The wear tests were conducted orthogonal to the build-up direction. To avoid damaging the cutting edge during tool entry, a roll-in entry was used. The tool was removed at regular intervals, and the tool wear was examined using optical microscopy (VHX6000, Keyence). To confirm the results, each machining test was repeated once. The tests on the samples were randomized to avoid systematic uncertainties. In addition, the resulting chips were examined by light microscopy (Aristomet, Leitz) and scanning electron microscopy (EVO 60, Zeiss). For the examinations, the chips were embedded, ground and polished (vibration polishing with $AlO_2$ suspension with grainsize <0.05 µm) and then etched with Kroll's reagent (6 ml $HNO_3$/3 ml HF/100 ml water). The scanning electron microscopy of the unprepared, cleaned chips was carried out on a Zeiss Evo 60.

## 3. Results and discussion

### 3.1. Material characterisation

The chemical analysis results presented in Table 1 indicate that the reference material, the utilized powder, and the additively

manufactured samples closely match the nominal composition of Ti-5553. For clarity, only the additively manufactured sample with the highest energy density ($E_V = 37.0$ J/mm$^3$) is included in the table. It is worth noting that with these parameters, potential evaporation processes or chemical alterations during the building process are more likely. However, for the metallic components, no significant changes attributable to the additive manufacturing process are observed compared to the initial Ti-5553 powder. The presence of copper contamination in the bulk Ti-5553 samples (both reference and additively manufactured) can be attributed to the subsequent preparation process involving wire erosion using a brass wire.

Analysis of the non-metallic components reveals nearly equal oxygen content, with slightly elevated nitrogen and carbon content compared to the conventionally fabricated reference material. Despite the manufacturing process occurring in an inert argon atmosphere, the possibility of oxidation, vaporization, and gas inclusions due to the melting process using laser radiation cannot be entirely eliminated [45].

In general, the aim was to produce additive samples consisting entirely of β-phase. Hence, high cooling rates, even with increasing height of the samples, are required to suppress the formation of α-titanium. The results of qualitative phase analyses by means of X-ray diffraction (XRD) are shown in Fig. 2. The reference material (Fig. 2a) shows several signals, which can be assigned mainly to the cubic β- and hexagonal α-phases of Ti-5553. In contrast, the used powder demonstrated clear reflections of β-titanium (Fig. 2b), with no other phases detected.

To determine a possible change in the phase composition over the component height, three different transverse sections of the samples at heights from the base plate of 15, 25, and 35 mm were prepared. This procedure was carried out for all investigated additive manufacturing process parameters. For simplicity, of the four process parameters, only the XRD results over the component height with the lowest (20.8 J/mm$^3$) and the highest energy input (37.0 J/mm$^3$) are presented (Fig. 2c, d). At first glance, the diagram shows that the β-structure could be maintained up to room temperature for the sample with 20.8 J/mm$^3$ at all positions investigated. However, peaks are partially broadened, especially in the highest measuring position and with the energy density of 32.7 J/mm$^3$ (data not shown here), which may indicate the presence of the α-phase.

The qualitative phase analysis of the sample 37.0 J/mm$^3$ indicates changes with increasing distance from the base plate (Fig. 2d). Here, the signals of the β-phase decrease and become significantly broader, and additional peaks arise, indicating the α-phase. One possible reason for the formation of the α-phase is the high energy input of the LPBF process used to produce these samples (Table 2). The energy density of sample 37.0 J/mm$^3$ shows the highest value of all examined samples. Thus, compared to the other samples, a temperature accumulation can occur with increasing distance from the base plate, whereby sufficiently high cooling rates are not achieved in the upper region of the specimen, leading to the formation of the α-phase due to aging processes. In conclusion, a gradient phase composition with increasing height is formed when applying high energy densities.

In Fig. 3, the phase maps of the respective samples analyzed by EBSD are shown. The top images depict an overview and detailed view of the conventionally manufactured reference sample, where the α-precipitates are clearly identifiable as green sub-grains. In contrast, the additively manufactured samples exhibit a predominantly uniform red coloration up to an energy density of 32.7 J/mm$^3$, indicating the presence of β-titanium. At an energy density of 37.0 J/mm$^3$, distinct green spots (α-phase) are visible within the red matrix (β-phase). This

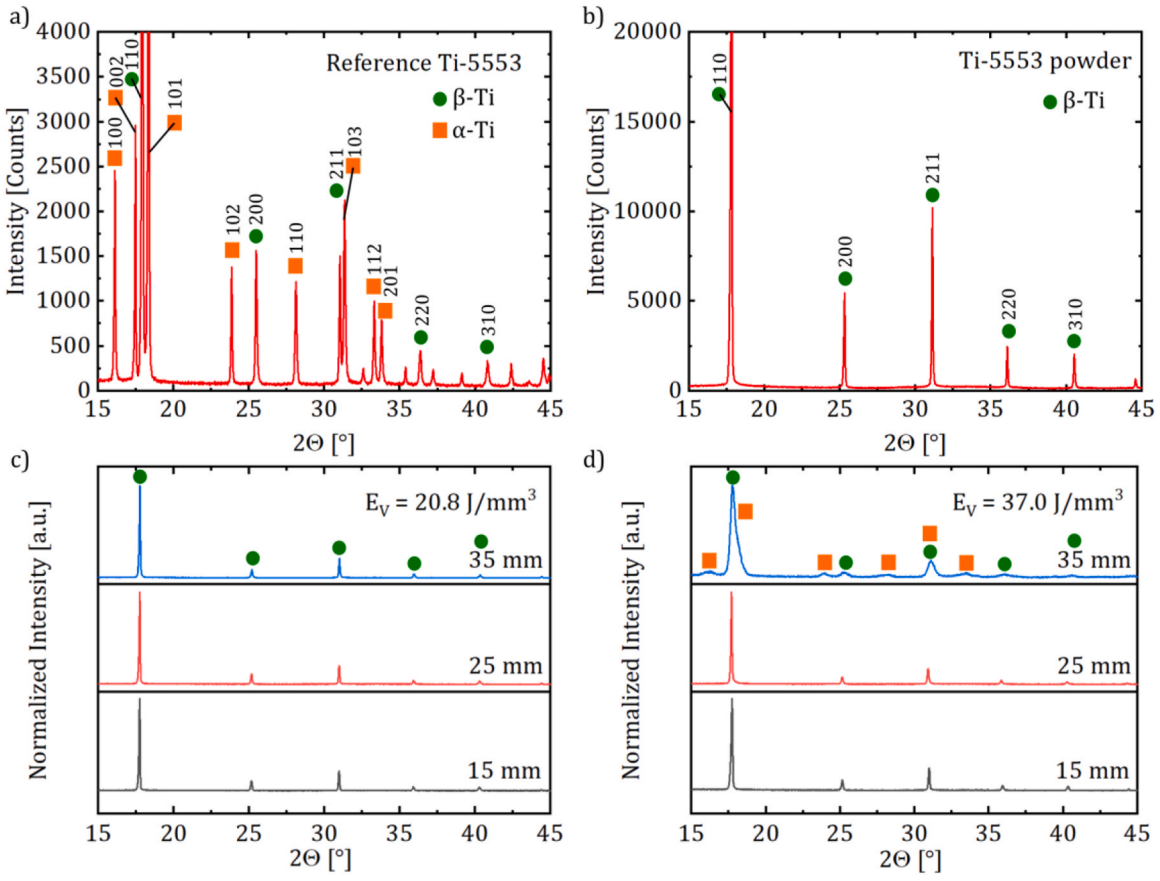


**Fig. 2.** Qualitative phase analysis results by XRD. a) Reference material and b) Ti-5553 powder. XRD patterns across the height of the additively manufactured samples with laser energy densities of c) 20.8 J/mm$^3$ and d) 37.0 J/mm$^3$. The intensity of AM samples was normalized to the maximum of the β110 reflection.

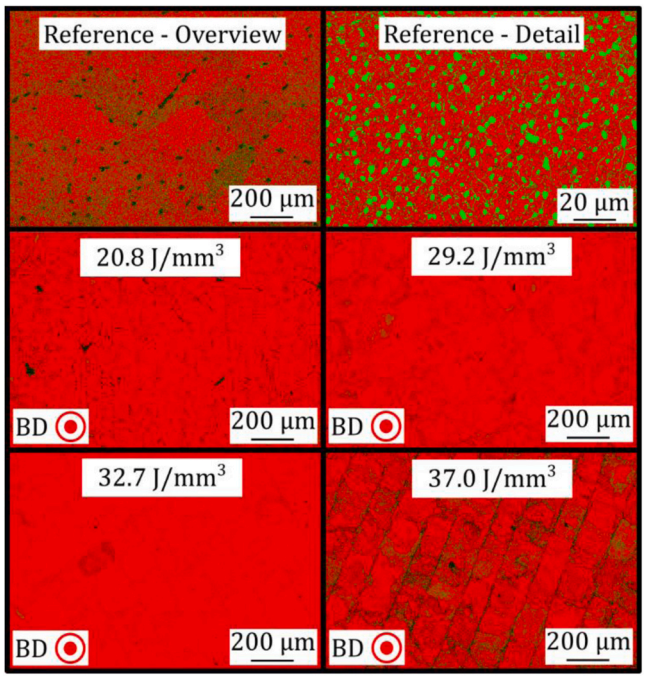


**Fig. 3.** EBSD phase maps of Ti-5553 samples (reference and additively manufactured). β-titanium is shown in red, and α-titanium in green.

result also corroborates the XRD findings presented in Fig. 2.

In addition, the samples were analyzed with respect to their microstructure (Fig. 4) using a procedure similar to that employed for phase analysis. As with the XRD characterization, different heights (15, 25, and 35 mm) were examined to perform EBSD both parallel and perpendicular to the building direction for each LBPF processing parameter. The orientation maps in Fig. 4 illustrate examples from the middle plane at a height of 25 mm. For comparative purposes, the microstructure of the conventionally produced sample is also shown. Again, the reference sample is characterized by a grain structure with globular segregation, representing a sub-grain structure of the α-phase resulting from heat treatment.

At first glance, the characteristic microstructure of additively manufactured components is evident, showcasing the typical grain shapes. Perpendicular to the building direction (view A), the stripe scan pattern of the laser is clearly visible. Parallel to the building direction (view B), the typical elongated grains of the microstructure are apparent. Sample 20.8 J/mm$^3$, which was produced with the lowest energy density and the highest volume rate, displays the smallest grain size among the additively manufactured samples. This small grain size can be attributed to the high cooling rates and low energy density of the LBPF process. As energy density increases, grain sizes also increase. For samples 29.2 J/mm$^3$ and 32.7 J/mm$^3$, there is no evidence of α-phase formation in the EBSD or XRD analysis despite the higher energy input compared to sample 20.8 J/mm$^3$. However, it is clear that the increased energy input and the associated higher heat lead to grain growth, resulting in a significantly coarser grain structure compared to sample 20.8 J/mm$^3$. These findings are consistent with the studies by Thijs *et al.* [12], which indicate that the lowest scanning velocity and thus the highest energy density result in a coarser grain structure. In general, when conducting EBSD analysis on additively manufactured microstructures, it is important to note that the evaluation can be quite challenging due to the process-induced anisotropies and heterogeneities [46]. Compared to conventionally manufactured materials [47–49], the microstructures often exhibit significantly lattice distortion and irregular grain shapes. As a result, categorizing or comparing these structures with other materials is only partially feasible.

The relative densities and mechanical properties of all investigated specimens are summarized in Table 3. For comparison, the properties of the conventionally produced material are also presented. Comparing the relative densities of the materials, it is evident that the sample produced with the lowest energy density (20.8 J/mm$^3$) exhibits the lowest relative density at 97.8%. As the energy input increases, the relative density also increases, reaching a maximum value of 99.4% at 37.0 J/mm$^3$. It is important to note that the additively manufactured samples are in their as-built state, while the reference material has undergone heat treatment. All additively manufactured samples exhibit reduced tensile strengths ($R_m$) and increased compressive strengths ($\sigma_{dB}$) compared to the reference sample.

Fig. 5 displays the mechanical properties of the additively manufactured samples as a function of the energy density of the LPBF process. It is evident that the tensile properties ($R_m$) of the additively manufactured samples are generally similar, though sample 20.8 J/mm$^3$ shows a slightly lower tensile strength compared to the other additively manufactured samples. This lower strength is attributed to the lowest energy input, which results in the presence of pores and lack of fusion in the component, adversely affecting the tensile strength. Consequently, the specimen with an energy density of 20.8 J/mm$^3$ demonstrates the lowest elongation at break, measuring 1.4 ± 0.2%.

Samples produced with higher energy densities exhibit similar engineering tensile strengths of around 825 MPa, which are lower than the tensile strength of the reference material. However, these samples have a higher maximum elongation at break compared to the reference. This is attributed to the absence of the α-phase in the additively manufactured specimens. At the highest energy density, the elongation at fracture decreases significantly due to the formation of the α-phase with increasing component height.

The strength values reported here are lower than those reported by Hendl *et al.* [50], but are consistent with the findings of Hicks *et al.* [51] in the as-built state. Hendl *et al.* produced samples using electron beam powder bed fusion and reheated the samples after each build cycle to maintain nearly constant process temperatures. This approach resulted in a microstructure with a higher proportion of the α-phase, which may account for the higher strength values. In contrast, Hicks *et al.* utilized laser metal deposition (LMD) without reheating steps after the build cycles, leading to a microstructure consisting entirely of the β-phase, which aligns with the findings of this work. Therefore, the mechanical properties are comparable.

The maximum compressive strength ($\sigma_{dB}$) initially shows a slight increase with rising energy density. However, with further increases in energy density, no significant change in maximum compressive strength is observed.

Microhardness measurements were performed along the building direction with a spacing of 1.5 mm between measurement points in the middle plane of the samples, as illustrated in Fig. 6. The reference sample has an average hardness of 338 ± 20 HV 0.2. The average hardness values for the additively manufactured samples are 294 ± 9 HV 0.2 for sample 20.8 J/mm$^3$, 301 ± 9 HV 0.2 for sample 29.2 J/mm$^3$, 311 ± 6 HV 0.2 for sample 32.7 J/mm$^3$, and 321 ± 35 HV 0.2 for sample 37.0 J/mm$^3$. These hardness values are comparable to those reported in previous studies on additively manufactured Ti-5553 [51].

As shown in Fig. 6, there is no significant difference in microhardness along the building direction for samples 20.8 J/mm$^3$, 29.2 J/mm$^3$ and 32.7 J/mm$^3$. However, the measurements indicate that the hardness values for sample 37.0 J/mm$^3$ tend to increase with distance from the base plate (Fig. 6).

Fig. 7 illustrates the microhardness as a function of the energy density of the LPBF process. With increasing energy density, the microhardness value rises, which is consistent with the findings of Thijs *et al.* [12] on the additive manufacturing of Ti-6Al-4V. It should be noted that due to changes in phase composition and microstructure within the component, the sample with the highest energy density of 37.0 J/mm$^3$ may exhibit variations in mechanical properties and microhardness that were not considered in this study. For the other

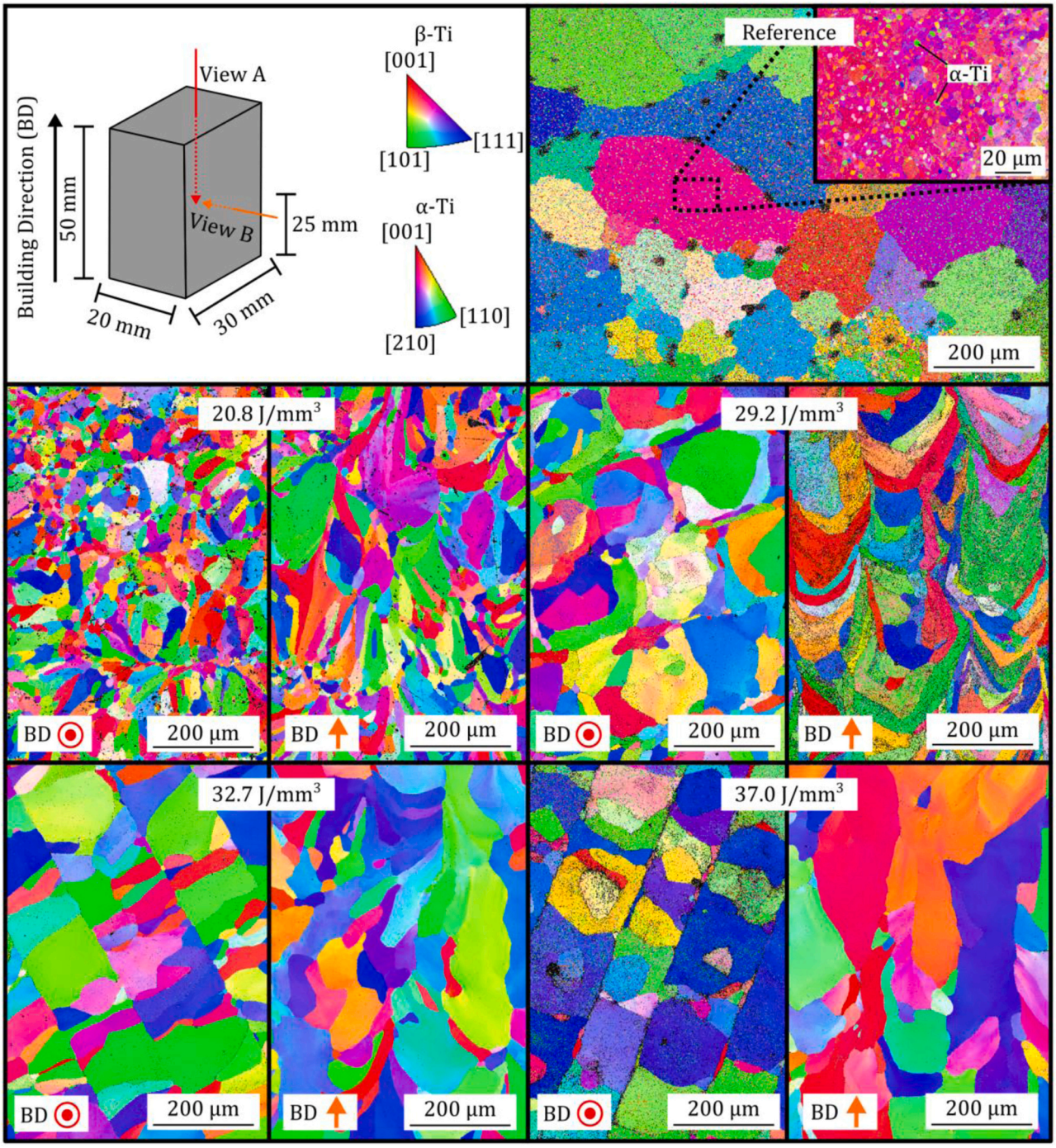


**Fig. 4.** Scheme showing the position of the sample extraction and EBSD orientation maps (z-direction) of the Ti-5553 reference sample and Ti-5553 LPBF samples, illustrating the microstructure both parallel and perpendicular to the building direction for various laser energy densities.

**Table 3**
Relative densities and mechanical properties of additively built Ti-5553 samples in comparison to the reference.

| Sample name | Relative density [%] | Eng.compressive strength $\sigma_{dB}$ [MPa] | Max. compressive strain at break $\varepsilon$ [%] | Eng. Tensile strength $R_m$ [MPa] | Max. elongation at break $A$ [%] | Microhard- ness [HV 0.2] |
|---|---|---|---|---|---|---|
| Reference | 99.8 ± 0.1 | 1913 ± 74 | 13.7 ± 3.2 | 1314 ± 12 | 3.7 ± 1.8 | 339 ± 20 |
| 20.8 J/mm³ | 97.8 ± 0.3 | 2141 ± 65 | 40.3 ± 1.1 | 746 ± 24 | 1.4 ± 0.2 | 294 ± 9 |
| 29.2 J/mm³ | 98.7 ± 0.1 | 2159 ± 15 | 39.8 ± 0.4 | 824 ± 19 | 6.1 ± 1.0 | 301 ± 9 |
| 32.7 J/mm³ | 99.3 ± 0.2 | 2181 ± 65 | 42.7 ± 2.5 | 826 ± 7 | 7.8 ± 1.8 | 311 ± 7 |
| 37.0 J/mm³ | 99.4 ± 0.1 | 2122 ± 38 | 38.5 ± 0.6 | 825 ± 10 | 1.8 ± 0.4 | 321 ± 36 |

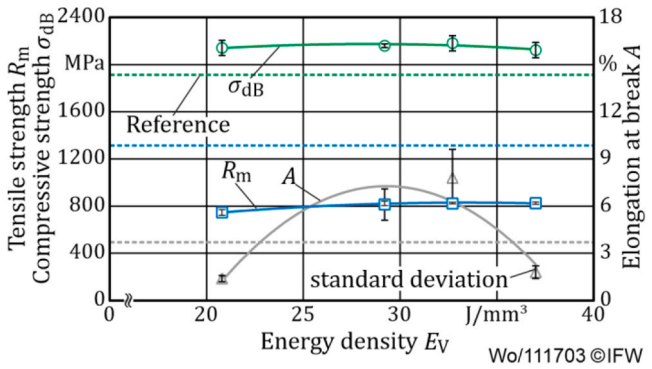


**Fig. 5.** Mechanical properties of Ti-5553 as a function of LPBF process energy densities.

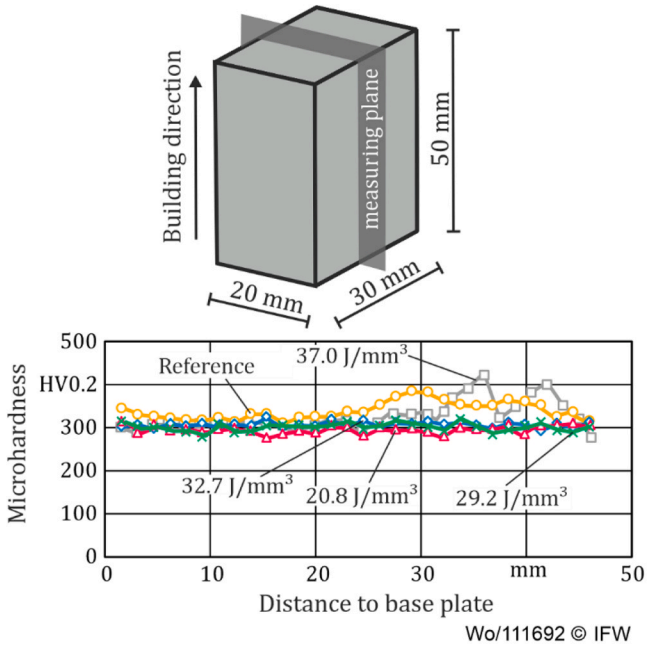


**Fig. 6.** Measurement positions and corresponding results of microhardness measurements for Ti-5553.

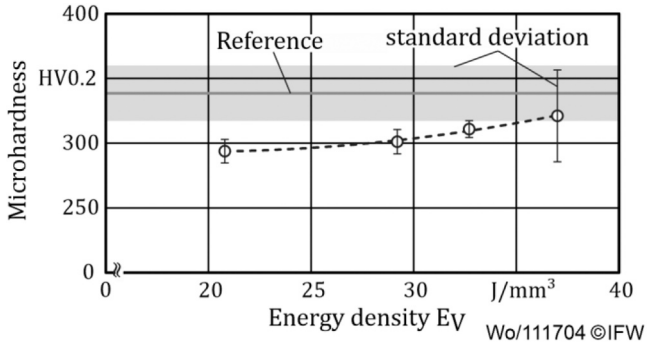


**Fig. 7.** Microhardness of Ti-5553 as a function of LPBF process energy density ($E_V$).

samples with lower energy inputs, a homogeneous microstructure and phase composition were observed, allowing for the assumption of uniform mechanical performance throughout the component.

### 3.2. Milling experiments

Following the sample characterisation, wear tests were conducted by milling both the reference and additively manufactured Ti-5553 samples with cemented carbide tools, as described in Section 2.2. Fig. 8 illustrates the development of the maximum width of the flank wear land on the tools over increasing cutting times. Each test was performed twice, and the repeat tests show good agreement, indicating high reliability of the results.

When milling the conventionally produced reference samples, a maximum tool life of 17.5 min was achieved. Tool life ended due to chipping of the cutting edge, with chips exceeding 200 µm in size (Fig. 9). Milling the additively manufactured sample with an energy density of 37.0 J/mm$^3$ also resulted in cutting-edge chipping, but in this case, tool life was reached after only 2.5 min of cutting time. This rapid tool wear for the 37.0 J/mm$^3$ samples may be attributed to the formation of fine α-phase precipitates in the areas furthest from the base plate.

These findings align with studies involving a substrate heating device during manufacturing [43]. The substrate heating device was set to 500 °C, which led to the precipitation of finely distributed, plate-like α-precipitates within the β-matrix. Milling these samples resulted in increased tool wear compared to conventionally manufactured and additively manufactured samples without substrate heating.

In contrast, the sample with an energy density of 32.7 J/mm$^3$ exhibited wear behaviour similar to the reference material. For samples with energy densities of 20.8 J/mm$^3$ and 29.2 J/mm$^3$ , there was a significant increase in tool life, with no significant wear observed even after more than 29 min of cutting time.

In addition to investigating tool wear, process forces were measured. Fig. 10 illustrates the development of the feed force ($F_f$) and the feed normal force ($F_{fN}$) for all tools, showing the average maximum values for tooth engagements. For clarity, error bars indicating the variation between trials have been omitted.

The measurements indicate that the microstructure of the materials does not significantly affect the feed forces. However, distinct differences in feed normal forces are observed across the different microstructures. Milling sample 37.0 J/mm$^3$ results in the highest feed forces. For the reference samples, the feed forces are at a similar level. Initially, after less than 5 min of cutting time, the feed forces for the reference sample are on average 5% higher than those for the additively manufactured samples (excluding sample 37.0 J/mm$^3$). As cutting time increases and tool wear progresses, this difference grows from 8% to 20%. This finding contrasts with literature reports, which generally state that process forces during the machining of additively manufactured alloys are higher than those for wrought materials. However, it should be noted that the literature studies typically refer to an (α + β) Ti-6Al-4V

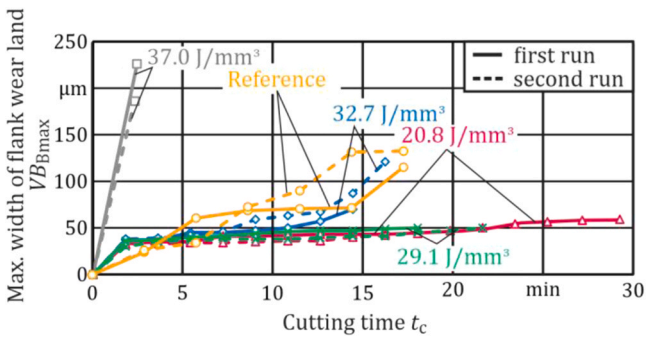


**Fig. 8.** Maximum width of flank wear land ($VB_{Bmax}$) of cemented carbide tools during the milling of Ti-5553 samples with various laser energy densities.

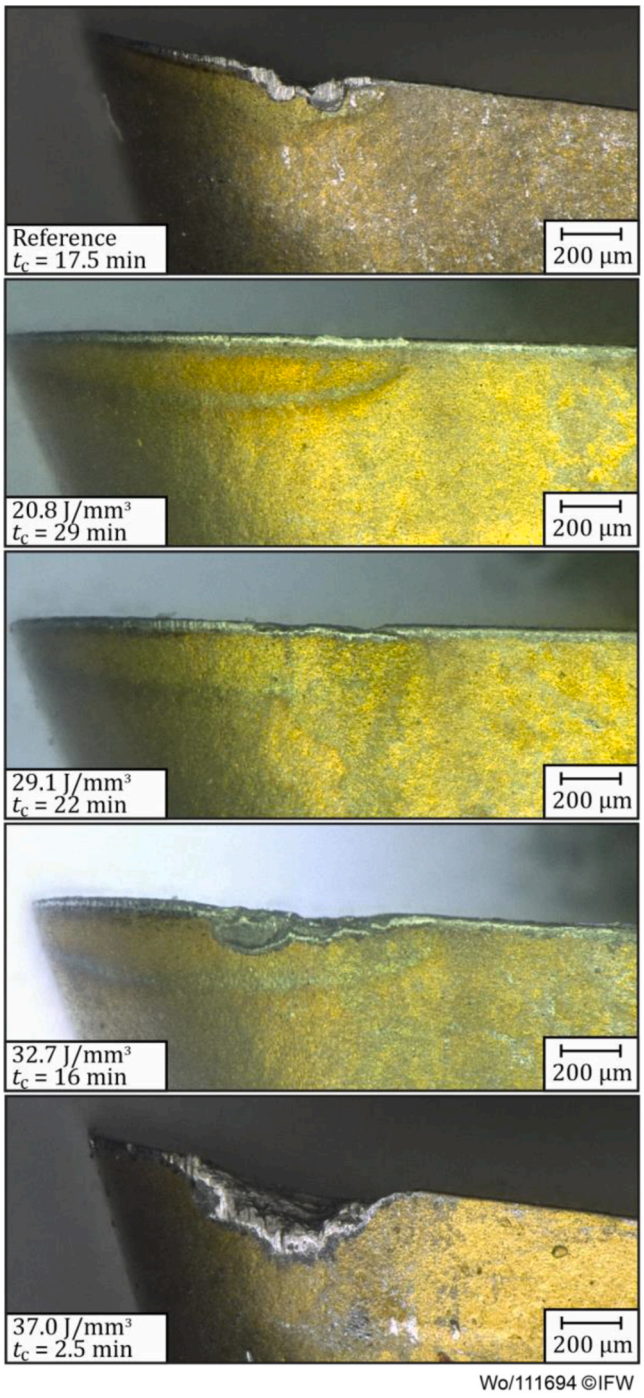


**Fig. 9.** Light microscopy images showing tool wear on cemented carbide tools during the milling of Ti-5553 samples with various laser energy densities.

alloy with different microstructure, and the specific manufacturing conditions and associated microstructural properties changes were not investigated. However, a major cause of the observed effects is the presence of α-titanium in both the reference sample and the 37.0 J/mm$^3$ sample. This explains the increased forces, as the α-phase of titanium has fewer slip systems. Additionally, the 37.0 J/mm$^3$ sample has a large grain size (Fig. 4), which may result in grains with an unfavorable orientation of the sliding planes being impacted during machining. This may lead to rapid tool failure and high process forces. Such an effect was also demonstrated in the investigations by Denkena and Grove [52], who found increased specific cutting forces when machining Ti-6Al-4V with a large grain size. Grove's research also showed that process

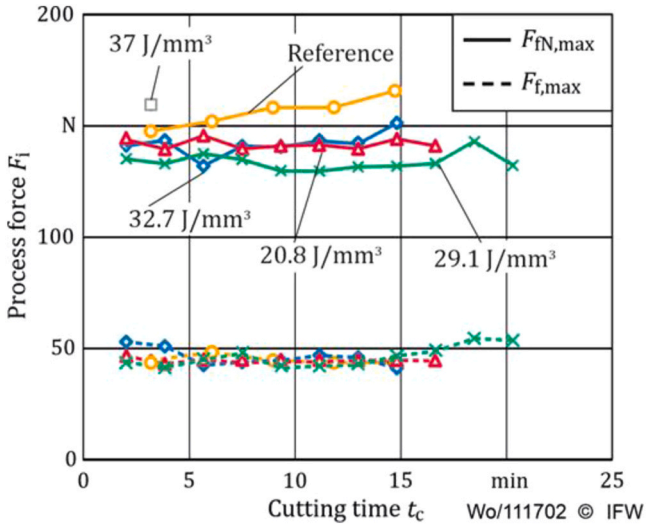


**Fig. 10.** Averaged peak values of process forces during the milling of Ti-5553 with various energy densities.

forces increase with a high proportion of α-titanium when machining Ti-6Al-4V.

When comparing the process forces for the additively manufactured specimens, the lowest feed forces are observed for sample 29.2 J/mm$^3$. This sample has a bidisperse beta-structure with both relatively coarse and fine grains. In contrast, the feed forces increase for sample 20.8 J/mm$^3$, despite its lower tensile strength compared to sample 29.2 J/mm$^3$. This may be due to the finer grain distribution perpendicular to the building direction and the higher grain boundary density in the feed direction for sample 20.8 J/mm$^3$, as shown in Fig. 4. The lower tensile strength of sample 20.8 J/mm$^3$, despite its smaller grain size, can be attributed to higher porosity (Table 3).

The feed forces for milling sample 32.7 J/mm$^3$ are similar to those of the samples from the 20.8 J/mm$^3$ test series. Sample 32.7 J/mm$^3$ has a coarser grain structure but higher strength, and the energy input during processing is similarly high as for sample 37.0 J/mm$^3$. Therefore, it cannot be conclusively determined from these results whether the cooling rates were sufficient to suppress α-phase formation. Further investigations, including a refined phase analysis using the Rietveld method, are necessary. The findings on the influence of energy density on the microstructural properties of AM Ti-5553 and associated tool wear phenomena represent a valuable extension of current research.

To better understand the tool wear behavior during the machining of different samples, the dynamics of the milling processes were analyzed through frequency analysis of force measurements using Fast Fourier Transformation (FFT). The FFT evaluation was conducted over 85 tool revolutions at the beginning of each tool's operating time to exclude wear-related influences on the frequency analysis. The results of the FFT for the frequency range up to 5 kHz are presented in Fig. 11.

It is evident that the lowest amplitudes are observed for the samples that exhibit the least tool wear (20.8 J/mm$^3$ and 32.7 J/mm$^3$). Notably, sample 37.0 J/mm$^3$, which causes the highest tool wear, shows increased amplitudes at both low and high frequencies. Increased amplitude values are also observed for sample 32.7 J/mm$^3$ and the reference sample, though they are significantly lower than those for sample 37.0 J/mm$^3$.

In summary, the dynamic force component increases with higher energy densities in the LPBF process, leading to accelerated tool wear. This observation aligns with Grove's findings on machining the alloy Ti-6Al-4V with various microstructural modifications [53]. Pouliquen *et al.* [54] reported higher frequencies of force signals during the machining of wrought Ti-5553 with an increased α-phase proportion. Therefore, the underlying mechanisms concerning the influence of microstructure

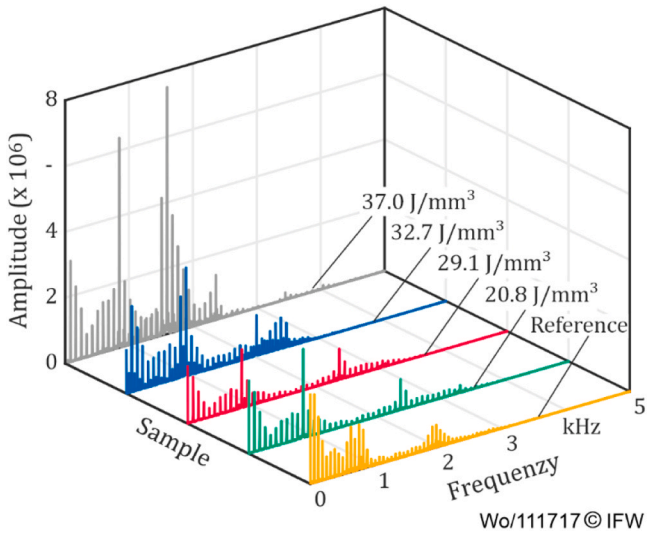


**Fig. 11.** FFT of the measured forces.

on dynamic process forces are comparable between wrought alloys and additively manufactured Ti-5553.

### 3.3. Investigations on chips

Due to the changed process parameters, it is expected that the produced samples have different thermomechanical properties. To investigate the effects of these properties on chip formation and tool wear, an analysis of the chips was carried out. Generally, chip formation in titanium alloys is characterized by the appearance of segmented chips, triggered by adiabatic shearing and cracking in the primary shear zone [30,55]. Depending on the combination of cutting speed and feed rate, aperiodic or periodic sliding of the chip segments occurs [56]. Systematic studies on the influence of microstructure modification on the chip formation of alloy Ti-5553 are not yet available.

The collected chips from the beginning of each milling experiment with a new tool are shown as scanning electron micrographs and optical microscopy images of the cross section in Figs. 12 and 13, respectively. The chips from the reference sample clearly show periodic sliding with chip segments extending across the chip's width. For the additively manufactured samples, periodic or aperiodic chip formation is detectable, depending on the energy density used in the LPBF process. Samples with relatively lower energy densities (20.8 J/mm$^3$, 29.1 J/mm$^3$, 32.7 J/mm$^3$) show aperiodic segmentation. The width of the segments varies significantly along the chip width, and the segments extend partially (32.7 J/mm$^3$) or not at all (20.8 J/mm$^3$ and 29.1 J/mm$^3$) across the full width of the chip (Fig. 12). The clearest localization of shear bands with segments along the whole width of the chip is seen in the 37.0 J/mm$^3$ sample and the wrought reference sample. Fig. 12 shows that both the reference sample and the sample produced with the highest energy density are characterized by comparable chip formation. This is caused by the presence of the α-phase, which is present in both samples. Similar effects were observed during the machining of wrought Ti-5553 with an increased proportion of the α-phase by Pouliquen *et al.* [54].

The hexagonal microstructure of α-titanium has fewer slip systems compared to the body-centered cubic crystal structure of the β-phase, making material deformation considerably more challenging, as indicated by the increased process forces in Fig. 10. According to Komanduri [57], this difficult deformability leads to an increase in local temperature, favouring adiabatic shearing and the formation of characteristic shear bands. This chip formation process is associated with increased tool wear [57]. These observations are consistent with the rapid tool wear observed when milling the 37.0 J/mm$^3$ sample. During chip

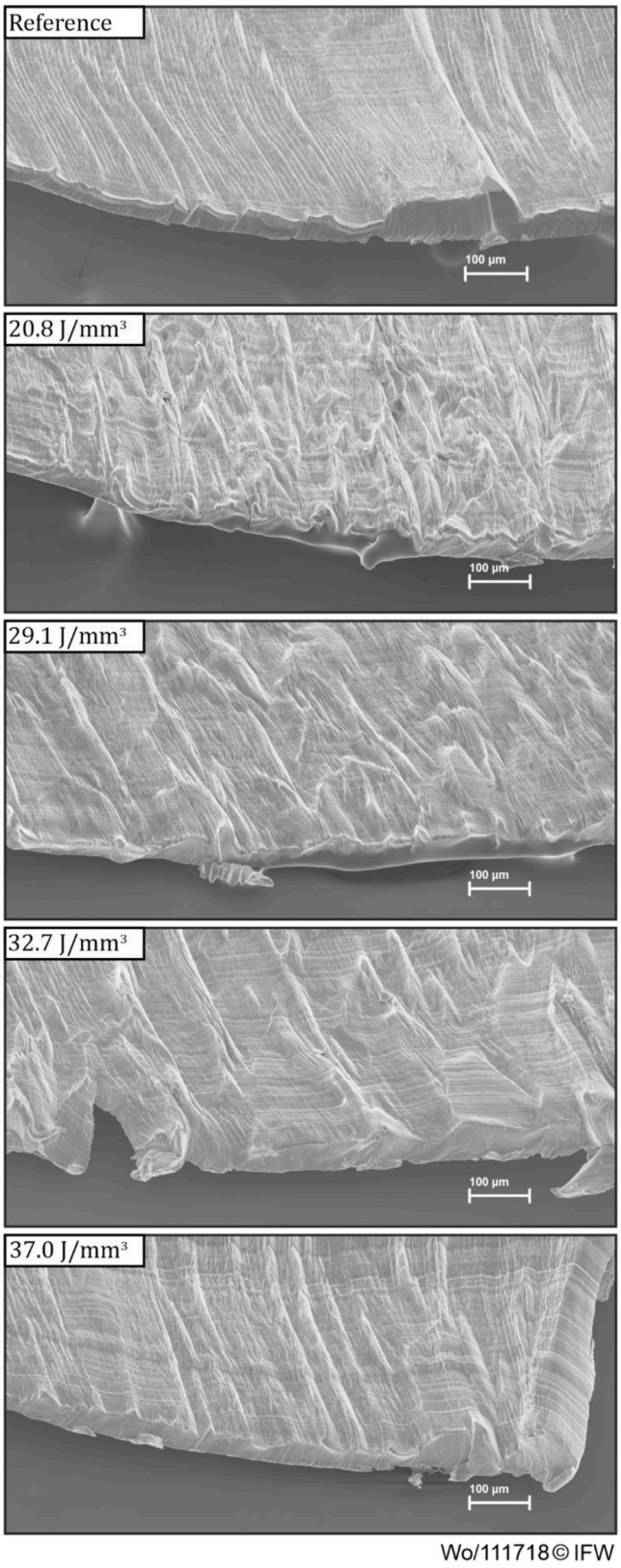


**Fig. 12.** Scanning electron micrographs of the chips from the reference material and built with different laser parameters.

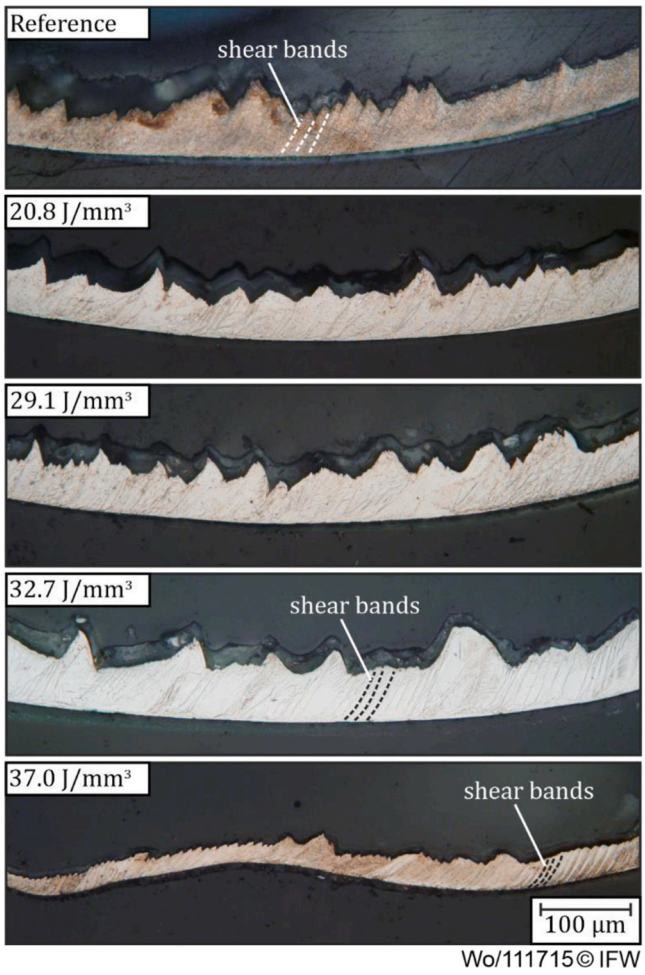


**Fig. 13.** Optical microscopy images of the chips from the reference and from LBPF samples.

formation, deformation energy is concentrated until failure occurs in the primary shear zone of the chip, subjecting the tool to a high dynamic load. This is also evident in the stronger dynamics of the force signal (Fig. 11).

Notably, the chips from specimens with higher tool wear (reference, 32.7 J/mm$^3$, 37.0 J/mm$^3$) show more pronounced shear bands, whereas specimens with lower tool wear show almost no shear bands (20.8 J/mm$^3$, 29.1 J/mm$^3$). These observations are consistent with studies by Barry *et al.* investigating chip formation in Ti-6Al-4V and hardened steel using acoustic emission (AE) [56]. Thus, a correlation between the investigated chip formation and the resulting tool wear can be verified.

## 4. Conclusion and outlook

This study examined how LPBF process parameters affect the machinability of additively manufactured Ti-5553 samples, comparing them to a wrought reference. Key findings include:

1. Process Parameters Impact: LPBF parameters significantly influence the microstructure and machinability of Ti-5553. Notably, samples produced with higher energy densities exhibit increased tool wear during milling.
2. Alpha Phase Formation: Elevated tool wear in high-energy-density samples is likely due to α-phase formation from higher temperatures and subsequent aging effects.
3. Force Implications: Microstructural variations affect feed normal force, though feed force remains unaffected during milling.
4. Chip Formation: Chip formation is significantly dependent on the microstructure of the material. The formation of shear bands is promoted by the presence of α-titanium.

Future research will focus more in detail on chip formation mechanisms, including generating chip roots through cut interruptions. Additionally, the influence of build-up direction on tool wear will be investigated as well as the impact of additional heat treatments of Ti-5553 on tool performance.

## Ethics approval

Not applicable.

## Funding

Funded by the Deutsche Forschungsgemeinschaft (DFG, German Research Foundation) – Project-ID 432764611.

## CRediT authorship contribution statement

**B. Denkena:** Conceptualization, Resources, Writing – original draft, Writing – review & editing, Supervision. **J.K. Hufenbach:** Conceptualization, Resources, Writing – original draft, Writing – review & editing, Supervision. **B. Bergmann:** Conceptualization, Writing – original draft, Writing – review & editing, Supervision. **U. Kühn:** Resources, Writing – review & editing. **A. Heckemeyer:** Formal analysis, Writing – review & editing, Visualization. **S. Worpenberg:** Conceptualization, Investigation, Formal analysis, Writing – original draft, Writing – review & editing, Visualization. **C. Kunz:** Conceptualization, Investigation, Formal analysis, Writing – original draft, Writing – review & editing, Visualization.

## Declaration of Competing Interest

The authors declare that they have no known competing financial interests or personal relationships that could have appeared to influence the work reported in this paper.

## Acknowledgement

The authors would like to thank T. Gustmann, A. Voß, K. Neufeld and K. Bretzke from IFW Dresden for technical support regarding the additive manufacturing facility, chemical analysis, EBSD analysis and characterization of mechanical properties.

*Code availability*

Not applicable.

*Consent to participate*

The authors declare that all authors have read and approved to submit this manuscript.

*Consent for publication*

The authors declare that all authors agree to sign the transfer of copyright for the publisher to publish this article upon acceptance.

## References

[1] DebRoy T, Wei HL, Zuback JS, Mukherjee T, Elmer JW, Milewski JO, et al. Additive manufacturing of metallic components – process, structure and properties. Progress in Materials Science 2018;92:112–224. https://doi.org/10.1016/j.pmatsci.2017.10.001.

[2] Gu DD, Meiners W, Wissenbach K, Poprawe R. Laser additive manufacturing of metallic components: materials, processes and mechanisms. International Materials Reviews 2012;57:133–64. https://doi.org/10.1179/1743280411y.0000000014.

[3] Bass N., J.S, Manogharan G. Net-Shape Tensile Specimens as Representatives of Mate-rial Properties of Metal Additive Manufacturing: Evalua-tion and Correction Factor. In Proceedings of the Proceedings of the ASME 2022 17th International Manu-facturing Science and Engineering Conference (MSEC2022), West Lafayette, Indiana, 2022.

[4] Liu SY, Li HQ, Qin CX, Zong R, Fang XY. The effect of energy density on texture and mechanical anisotropy in selective laser melted Inconel 718 (doi) Materials & Design 2020;191:108642. https://doi.org/10.1016/j.matdes.2020.108642.

[5] Ciurana J, Hernandez L, Delgado J. Energy density analysis on single tracks formed by selective laser melting with CoCrMo powder material. The International Journal of Advanced Manufacturing Technology 2013;68:1103–10. https://doi.org/10.1007/s00170-013-4902-4.

[6] Monteiro H, Carmona-Aparicio G, Lei I, Despeisse M. Energy and material efficiency strategies enabled by metal additive manufacturing – a review for the aeronautic and aerospace sectors. Energy Reports 2022;8:298–305. https://doi.org/10.1016/j.egyr.2022.01.035.

[7] Liu S, Shin YC. Additive manufacturing of Ti6Al4V alloy: a review. Materials & Design 2019;164:107552. https://doi.org/10.1016/j.matdes.2018.107552.

[8] Daniel Elitzer SJ, Clara Höll, Daniel Baier, Rosa Varga, Zaeh Michael F, Göken Mathias, et al. Development of microstructure and mechanical properties of TiAl6V4 processed by wire and Arc additive manufacturing. Advanced Engineering Materials 2022;25:2201025. https://doi.org/10.1002/adem.202201025.

[9] DebRoy T, Mukherjee T, Milewski JO, Elmer JW, Ribic B, Blecher JJ, et al. Scientific, technological and economic issues in metal printing and their solutions. Nature Materials 2019;18:1026–32. https://doi.org/10.1038/s41563-019-0408-2.

[10] Liu K, Gu D, Guo M, Sun J. Effects of processing parameters on densification behavior, microstructure evolution and mechanical properties of W–Ti alloy fabricated by laser powder bed fusion. Materials Science and Engineering: A 2022;829:142177. https://doi.org/10.1016/j.msea.2021.142177.

[11] Qiu C, Ravi GA, Attallah MM. Microstructural control during direct laser deposition of a β-titanium alloy. Materials & Design 2015;81:21–30. https://doi.org/10.1016/j.matdes.2015.05.031.

[12] Thijs L, Verhaeghe F, Craeghs T, Humbeeck JV, Kruth J-P. A study of the microstructural evolution during selective laser melting of Ti–6Al–4V. Acta Materialia 2010;58:3303–12. https://doi.org/10.1016/j.actamat.2010.02.004.

[13] Bakhshivash S, Asgari H, Russo P, Dibia CF, Ansari M, Gerlich AP, et al. Printability and microstructural evolution of Ti-5553 alloy fabricated by modulated laser powder bed fusion. The International Journal of Advanced Manufacturing Technology 2019;103:4399–409. https://doi.org/10.1007/s00170-019-03847-3.

[14] Xu W, Brandt M, Sun S, Elambasseril J, Liu Q, Latham K, et al. Additive manufacturing of strong and ductile Ti–6Al–4V by selective laser melting via in situ martensite decomposition. Acta Materialia 2015;85:74–84. https://doi.org/10.1016/j.actamat.2014.11.028.

[15] Wu L, Das S, Gridin W, Leuders S, Kahlert M, Vollmer M, et al. Hot work tool steel processed by laser powder bed fusion: a review on most relevant influencing factors. Advanced Engineering Materials 2021;23:2100049. https://doi.org/10.1002/adem.202100049.

[16] Schwab H, Palm F, Kühn U, Eckert J. Microstructure and mechanical properties of the near-beta titanium alloy Ti-5553 processed by selective laser melting. Materials & Design 2016;105:75–80. https://doi.org/10.1016/j.matdes.2016.04.103.

[17] Vrancken B, Thijs L, Kruth J-P, Van Humbeeck J. Heat treatment of Ti6Al4V produced by selective laser melting: microstructure and mechanical properties. Journal of Alloys and Compounds 2012;541:177–85. https://doi.org/10.1016/j.jallcom.2012.07.022.

[18] Zhang J, Bermingham MJ, Otte J, Liu Y, Hou Z, Yang N, et al. Ultrauniform, strong, and ductile 3D-printed titanium alloy through bifunctional alloy design. Science 2024;383:639–45. https://doi.org/10.1126/science.adj0141.

[19] Pilz S, Gustmann T, Günther F, Zimmermann M, Kühn U, Gebert A. Controlling the Young's modulus of a ß-type Ti-Nb alloy via strong texturing by LPBF. Materials & Design 2022;216:110516. https://doi.org/10.1016/j.matdes.2022.110516.

[20] Gu D. Laser Additive Manufacturing of High-Performance Materials. Springer: Heidelberg,; 2015.

[21] Sander J, Hufenbach J, Giebeler L, Wendrock H, Kühn U, Eckert J. Microstructure and properties of FeCrMoVC tool steel produced by selective laser melting. Materials & Design 2016;89:335–41. https://doi.org/10.1016/j.matdes.2015.09.148.

[22] Li CC, Xin C, Wang Q, Ren JQ, Zhao B, Wu JP, et al. A novel low-cost high-strength β titanium alloy: microstructure evolution and mechanical behavior. Journal of Alloys and Compounds 2023;959:170497. https://doi.org/10.1016/j.jallcom.2023.170497.

[23] Denkena B, Wichmann M, Pillkahn P. Effect of mechanical finishing on residual stresses and application behavior of wire arc additive manufactured aluminum components. Procedia CIRP 2022;108:135–40. https://doi.org/10.1016/j.procir.2022.03.026.

[24] King WE, Anderson AT, Ferencz RM, Hodge NE, Kamath C, Khairallah SA, et al. Laser powder bed fusion additive manufacturing of metals; physics, computational, and materials challenges. Applied Physics Reviews 2015;2. https://doi.org/10.1063/1.4937809.

[25] Klocke F, Krämer A, Sangermann H, Lung D. Thermo-mechanical tool load during high performance cutting of hard-to-cut materials. Procedia CIRP 2012;1:295–300. https://doi.org/10.1016/j.procir.2012.04.053.

[26] Lütjering, G.; Williams, J.C. *Titanium*; Springer Berlin Heidelberg: 2013.

[27] Rahman M, Wong YS, Zareena AR. Machinability of titanium alloys. JSME International Journal Series C Mechanical Systems, Machine Elements and Manufacturing 2003;46:107–15. https://doi.org/10.1299/jsmec.46.107.

[28] Hariharan A, Goldberg P, Gustmann T, Maawad E, Pilz S, Schell F, et al. Designing the microstructural constituents of an additively manufactured near β Ti alloy for an enhanced mechanical and corrosion response. Materials & Design 2022;217:110618. https://doi.org/10.1016/j.matdes.2022.110618.

[29] Pollock TM. Alloy design for aircraft engines. Nature Materials 2016;15:809–15. https://doi.org/10.1038/nmat4709.

[30] dos Santos RG, He Q, de Paiva JMF, Veldhuis SC, Torres RD, Amorim FL. A review on machining Ti–5Al–5V–5Mo–3Cr alloy using defined geometry tools. The International Journal of Advanced Manufacturing Technology 2024;131:3373–400. https://doi.org/10.1007/s00170-024-13237-z.

[31] Khatri N, Barkachary BM, Singh S, Manjunath K, Chandra N, Armstrong J, et al. Diamond machining of additively manufactured Ti6Al4V ELI: Newer mode of material removal challenging the current simulation tools. Journal of Manufacturing Processes 2024;120:378–90. https://doi.org/10.1016/j.jmapro.2024.04.051.

[32] Manjunath K, Tewary S, Khatri N, Cheng K. Simulation-based investigation on ultra-precision machining of additively manufactured Ti-6Al-4V ELI alloy and the associated experimental study. Proceedings of the Institution of Mechanical Engineers, Part B: Journal of Engineering Manufacture 2023;0:09544054231196920. https://doi.org/10.1177/09544054231196920.

[33] Farooq MU, Anwar S, Ullah R, Guerra RH. Sustainable machining of additive manufactured SS-316L underpinning low carbon manufacturing goal. Journal of Materials Research and Technology 2023;24:2299–318. https://doi.org/10.1016/j.jmrt.2023.03.122.

[34] Laue R, Colditz P, Möckel M, Awiszus B. Study on the milling of additive manufactured components. Metals 2022;12:1167.

[35] Khanna N, Zadafiya K, Patel T, Kaynak Y, Rahman Rashid RA, Vafadar A. Review on machining of additively manufactured nickel and titanium alloys. Journal of Materials Research and Technology 2021;15:3192–221. https://doi.org/10.1016/j.jmrt.2021.09.088.

[36] Li G, Chandra S, Rahman Rashid RA, Palanisamy S, Ding S. Machinability of additively manufactured titanium alloys: a comprehensive review. Journal of Manufacturing Processes 2022;75:72–99. https://doi.org/10.1016/j.jmapro.2022.01.007.

[37] Kishawy HA, Nguyen N, Hosseini A, Elbestawi M. Machining characteristics of additively manufactured titanium, cutting mechanics and chip morphology. CIRP Annals 2023;72:49–52. https://doi.org/10.1016/j.cirp.2023.04.056.

[38] Uçak N, Outeiro J, Çiçek A, Aslantas K. Comparative analysis of micro-milling performances of conventionally and additively manufactured Ti6Al4V alloys: experimental investigation and 3D modelling. CIRP Journal of Manufacturing Science and Technology 2024;51:213–35. https://doi.org/10.1016/j.cirpj.2024.05.003.

[39] Liu CZ, Wang L, Xu X. The effect of heat treatment on the microstructures and dynamic mechanical properties of near-β Ti-5553 alloy. Applied Mechanics and Materials 2015;782:137–42. https://doi.org/10.4028/www.scientific.net/AMM.782.137.

[40] Dehghan-Manshadi A, Dippenaar RJ. Development of α-phase morphologies during low temperature isothermal heat treatment of a Ti–5Al–5Mo–5V–3Cr alloy. Materials Science and Engineering: A 2011;528:1833–9. https://doi.org/10.1016/j.msea.2010.09.061.

[41] Kolli RP, Devaraj A. A review of metastable beta titanium alloys. Metals 2018;8:506.

[42] Ramachandiran N, Asgari H, Dibia F, Eybel R, Gerlich A, Toyserkani E. Effect of non-lamellar α precipitate morphology on the mechanical properties of Ti5553 parts made by laser powder-bed fusion at high laser scan speeds. Materials Science and Engineering: A 2022;841:143039. https://doi.org/10.1016/j.msea.2022.143039.

[43] Grove T, Denkena B, Maiß O, Krödel A, Schwab H, Kühn U. Cutting mechanism and surface integrity in milling of Ti-5553 processed by selective laser melting. Journal of Mechanical Science and Technology 2018;32:4883–92. https://doi.org/10.1007/s12206-018-0936-8.

[44] Schwab H, Prashanth KG, Löber L, Kühn U, Eckert J. Selective laser melting of Ti-45Nb alloy. Metals 2015;5:686–94.

[45] Liu J, Wen P. Metal vaporization and its influence during laser powder bed fusion process. Materials & Design 2022;215:110505. https://doi.org/10.1016/j.matdes.2022.110505.

[46] Kok Y, Tan XP, Wang P, Nai MLS, Loh NH, Liu E, et al. Anisotropy and heterogeneity of microstructure and mechanical properties in metal additive manufacturing: A critical review. Materials & Design 2018;139:565–86. https://doi.org/10.1016/j.matdes.2017.11.021.

[47] Khajuria A, Akhtar M, Bedi R, Kumar R, Ghosh M, Das CR, et al. Influence of boron on microstructure and mechanical properties of Gleeble simulated heat-affected zone in P91 steel. International Journal of Pressure Vessels and Piping 2020;188:104246. https://doi.org/10.1016/j.ijpvp.2020.104246.

[48] Khajuria A, Akhtar M, Bedi R, Kumar R, Ghosh M, Das CR, et al. Microstructural investigations on simulated intercritical heat-affected zone of boron modified P91-steel. Materials Science and Technology 2020;36:1407–18. https://doi.org/10.1080/02670836.2020.1784543.

[49] Khajuria A, Shiva S, Misra A. The carbon content effect on hot-rolled C–Mn micro-alloyed E410 structural steel. Vacuum 2023;212:112042. https://doi.org/10.1016/j.vacuum.2023.112042.

[50] Hendl J, Marquardt A, Leyens C. Electron beam powder bed fusion manufacturing of a Ti-5Al-5Mo-$^{5}$V–$^{3}$Cr alloy: a microstructure and mechanical properties'

correlation study. Progress in Additive Manufacturing 2023;8:459–75. https://doi.org/10.1007/s40964-022-00338-y.
[51] Hicks C, Sivaswamy G, Konkova T, Blackwell P. Anisotropic tensile properties and failure mechanism of laser metal deposited Ti–5Al–5Mo–5V–3Cr alloy before and after sub-transus heat-treatment. Materials Science and Engineering: A 2021;825:141928. https://doi.org/10.1016/j.msea.2021.141928.
[52] Denkena B, Grove T. The effect of microstructure on the machinability of Ti-6Al-4V. In *Proceedings of the 13th World Conference on Titanium* 2016:905–10.
[53] Grove, T.. Hochleistungszerspanung von Titan; PZH-Verl.: Garbsen, 2015.
[54] Pouliquen A, Chanfreau N, Gallegos-Mayorga L, Mareau C, Ayed Y, Germain G, et al. Influence of the microstructure of a Ti5553 titanium alloy on chip morphology and cutting forces during orthogonal cutting. Journal of Materials Processing Technology 2023;319:118054. https://doi.org/10.1016/j.jmatprotec.2023.118054.
[55] Gao Y, Wang G, Liu B. Chip formation characteristics in the machining of titanium alloys: a review. International Journal of Machining and Machinability of Materials 2016;18:155–84. https://doi.org/10.1504/ijmmm.2016.075467.
[56] Barry J, Byrne G, Lennon D. Observations on chip formation and acoustic emission in machining Ti–6Al–4V alloy. International Journal of Machine Tools and Manufacture 2001;41:1055–70. https://doi.org/10.1016/S0890-6955(00)00096-1.
[57] Komanduri R. Some clarifications on the mechanics of chip formation when machining titanium alloys. Wear 1982;76:15–34. https://doi.org/10.1016/0043-1648(82)90113-2.